Reverberant shear wave fields and estimation of tissue properties

Kevin J Parker[1]**, Juvenal Ormachea**[1]**, Fernando Zvietcovich**[1] **and Benjamin Castaneda**[2]

[1] Department of Electrical and Computer Engineering, University of Rochester, Hopeman Building, Box 270126, Rochester, NY 14627, USA
[2] Laboratorio de Imágenes Médicas, Pontificia Universidad Católica del Perú, Av. Universitaria 1801, San Miguel Lima 32, Peru

E-mail: kevin.parker@rochester.edu

Abstract

The determination of shear wave speed is an important subject in the field of elastography, since elevated shear wave speeds can be directly linked to increased stiffness of tissues. MRI and ultrasound scanners are frequently used to detect shear waves and a variety of estimators are applied to calculate the underlying shear wave speed. The estimators can be relatively simple if plane wave behavior is assumed with a known direction of propagation. However, multiple reflections from organ boundaries and internal inhomogeneities and mode conversions can create a complicated field in time and space. Thus, we explore the mathematics of multiple component shear wave fields and derive the basic properties, from which efficient estimators can be obtained. We approach this problem from the historic perspective of reverberant fields, a conceptual framework used in architectural acoustics and related fields. The framework can be recast for the alternative case of shear waves in a bounded elastic media, and the expected value of displacement patterns in shear reverberant fields are derived, along with some practical estimators of shear wave speed. These are applied to finite element models and phantoms to illustrate the characteristics of reverberant fields and provide preliminary confirmation of the overall framework.

Keywords: elastography, shear waves, tissue stiffness, reverberant fields, shear wave speed estimators, MRE, ultrasound

(Some figures may appear in colour only in the online journal)

1. Introduction

There has been a robust development of techniques to estimate and image the biomechanical properties of tissues (Parker *et al* 2011). One way to categorize the more widely used approaches is by the class of applied stimulus: quasi-static, transient, or continuous waves. Each one of these has unique mathematics and techniques for inverse solutions (Doyley 2012), but all lie on a continuum of biomechanical responses (Parker *et al* 2005, Parker 2013). Shear wave propagation has received significant attention, but an inherent problem in many approaches is the presence of reflected waves from organ boundaries and internal inhomogeneities. These reflections are responsible for modal patterns (Parker and Lerner 1992, Taylor *et al* 2000) in continuous wave applications and also for backwards travelling waves in transient experiments (Ringleb *et al* 2005). Directional filtering can be used to eliminate some types of reflections (Manduca *et al* 2003, McLaughlin and Renzi 2006, Deffieux *et al* 2011, Hah *et al* 2012, Pengfei *et al* 2012, Engel and Bashford 2015, Castaneda *et al* 2009).

Many continuous shear wave inversion approaches have been developed to estimate the unknown tissue stiffness. These would include inversions of the Helmoltz equation in magnetic resonance elastography (MRE) (Romano *et al* 2000, Sinkus *et al* 2000, Oliphant *et al* 2001, Van Houten *et al* 2001, Ringleb *et al* 2005) and sonoelastography (Parker and Lerner 1992, Fai *et al* 1998, Fu *et al* 1999). Another class of estimations has been developed for underwater acoustics and geomechanics using random signals (Roux *et al* 2005) and these have been extended to noise correlation measurements in soft tissues (Catheline *et al* 2008, Gallot *et al* 2011, Brum *et al* 2015). These involve spatial coherence of noise functions measured at two points, and can be recast as Green's functions and time reversal solutions.

Furthermore, an approach using a mechanical vibration source to produce multiple wave directions in a large organ such as the liver, has been developed by Tzschatzsch *et al* (2014, 2015, 2016). Using a probability approach, they characterize the shear wave speed (SWS) by finding the minimum wavenumber as a function of direction.

In this work we take an alternative path, applying the concept of a narrow-band reverberant field of many waves within tissue. These are naturally established (even unavoidable) in practical situations, and can be reinforced by utilizing multiple shear sources near the tissues of interest. This particular approach leads to simple solutions, facile implementation, and rapid estimation of local tissue shear wavelength or SWS.

2. Theory

The complex pressure $\widehat{P}$ at a position ε in a reverberant chamber can be thought of as the superposition of plane waves incident from all directions (Pierce 1981, Parker and Maye 1984)

$$\widehat{P}(t, \varepsilon) = \sum_q \widehat{P}_q \exp\left[j(k\mathbf{n}_q \cdot \varepsilon - \omega_0 t)\right] , \tag{1}$$

where the index q represents direction, $\mathbf{n}_q$ are unit vectors uniformly distributed around 4π solid angle, k and ω are the wave number and radial frequency of the plane waves, and $\widehat{P}_q$ are independent, identically distributed variables of random magnitude and phase. The corresponding velocity at a point is thereby given as

$$\mathbf{v}(t, \varepsilon) = \sum_q \mathbf{n}_q \widehat{\upsilon}_q \exp\left[j(k\mathbf{n}_q \cdot \varepsilon - \omega_0 t)\right] , \tag{2}$$

where from the plane-wave impedance relations

$$\widehat{\upsilon}_q = \boldsymbol{n}_q \widehat{P}_q / \rho c, \tag{3}$$

where ρ is the media density, and c the speed of sound.

In order to calculate the autocorrelation function, we write the x component of velocity at some position ε within the tissue:

$$\widehat{\upsilon}_x(\varepsilon) = \mathbf{e}_x \cdot \mathbf{v}(\varepsilon) = \sum_q n_{xq} \widehat{\upsilon}_q \exp\left[j\big(k\mathbf{n}_q \cdot \varepsilon - \omega_0 t\big) \right], \tag{4}$$

where $\hat{\mathbf{e}}_x$ is a unit vector in the x direction and

$$n_{xq} = \mathbf{n}_q \cdot \hat{\mathbf{e}}_x. \tag{5}$$

The summation on q is understood to be taken over 4π solid angle.

By writing the correlation function definition then substituting equation (4), we obtain:

$$B\upsilon_x\upsilon_x(\Delta t, \Delta\varepsilon) = E\{\widehat{\upsilon}_x(t,\varepsilon)\widehat{\upsilon}_x^*(t + \Delta t, \varepsilon + \Delta\varepsilon)\}$$

$$= E\Bigg\{ \left(\sum_q n_{xq} \widehat{\upsilon}_q \exp\left[j\big(k\mathbf{n}_q \cdot \varepsilon - \omega_0 t\big) \right] \right)$$

$$\times \left(\sum_{q'} n_{xq'} \widehat{\upsilon}_{q'}^* \exp\left\{ -j\left[k\mathbf{n}_{q'} \cdot (\varepsilon + \Delta\varepsilon) - \omega_0(t + \Delta t) \right] \right\} \right) \Bigg\}, \tag{6}$$

where $E\{\}$ represents an ensemble average and the asterisk represents conjugation. The product of the two series will include cross terms of the form:

$$E\{n_{xq}\widehat{\upsilon}_q n_{xq'}\widehat{\upsilon}_{q'}^* e^{(\cdots)}\} \tag{7}$$

But since the n_{xq} and $\widehat{\upsilon}_q$ are independent and the $\widehat{\upsilon}_q$ are uncorrelated, this term vanishes. Thus:

$$B\upsilon_x\upsilon_x(\Delta t, \Delta\varepsilon) = E\Bigg\{ \sum_q n_{xq}^2 \upsilon_q^2 \exp\left[j\big(\omega_0\Delta t - k\mathbf{n}_q \cdot \Delta\varepsilon\big) \right] \Bigg\}. \tag{8}$$

Taking the real part of the equation (8), we obtain:

$$B\upsilon_x\upsilon_x(\Delta t, \Delta\varepsilon) = (V^2)_{\mathrm{avg}} E\Bigg\{ \sum_q n_{xq}^2 \cos\big(\omega_0\Delta t - k\mathbf{n}_q \cdot \Delta\varepsilon\big) \Bigg\}, \tag{9}$$

where, since the V_q are independent of the n_{qx} and cosine terms; we have taken the mean squared value of the velocity out from the curly braces. Since an ideal, diffuse field is assumed to be present in the reverberant chamber, then the ensemble or spatial averaging will assign equal weighting to all directions of incident sound. Thus, the average of the summation over discrete directions becomes the average over all directions of incident waves (Cook *et al* 1955, Pierce 1981), around the polar coordinates of figure 1:

$$B\upsilon_x\upsilon_x(\Delta t, \Delta\varepsilon) = \frac{(V^2)_{\mathrm{avg}}}{2\pi} \int_{\mathrm{sphere}} n_{xq}^2 \cos\big(\omega_0\Delta t - k\mathbf{n}_q \cdot \Delta\varepsilon\big)\mathrm{d}\Omega. \tag{10}$$

Without loss of generality, we align the vector $\Delta\varepsilon$ with the z axis in figure 1. Using spherical coordinates:

$$\mathbf{n}_q \cdot \Delta\varepsilon_z = \Delta\varepsilon_z \cos\theta, \text{ and} \tag{11}$$
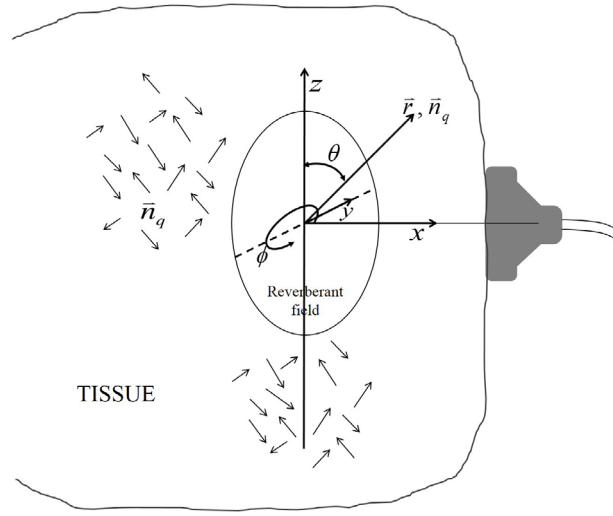
Figure 1. Schematic for the orientation of the imaging transducer (right), and the object that has an isotropic random distribution of shear waves propagating through the interior, consistent with the theory of reverberant fields. The *x*-axis of the coordinate system is aligned with the axial direction of the imaging transducer, and it is assumed that the imaging system detects motion in the *x*-direction. The $\bar{n}_q$ are the direction vectors of the individual plane waves that are distributed throughout the reverberant interior.

$$(n_{xq})^2 = (\mathbf{n}_q \cdot \hat{\mathbf{e}}_x)^2 = (\sin\theta\cos\phi)^2, \tag{12}$$

and the differential solid angle is

$$d\Omega = \sin\theta d\theta d\phi, \tag{13}$$

so

$$B\upsilon_x\upsilon_x(\Delta t, \Delta\varepsilon_z) = \frac{(V^2)_{\mathrm{avg}}}{2\pi}\int_{\phi=0}^{2\pi}\int_{\theta=0}^{\pi}(\sin\theta\cos\phi)^2\times\cos(\omega_0\Delta t - k\Delta\varepsilon_z\cos\theta)\sin\theta d\theta d\phi. \tag{14}$$

Integrating first over ϕ and expanding the cosine term yields

$$= 2\pi(V^2)_{avg}\left(\frac{j_1(k\Delta\varepsilon_z)}{k\Delta\varepsilon_z}\right)\cos\omega_0\Delta t \tag{15}$$

where $j_1(x)$ is the spherical Bessel function of the first kind, of order 1. This result is commensurate with the role of spherical Bessel functions in solutions to the Helmholtz equation via Fourier and Hankel transformations (Baddour 2011). Also, equation (15) can be written in terms of trigonometric functions or Bessel functions of order 3/2 (Abramowitz and Stegun 1964, Parker and Maye 1984).

Now, switching to shear waves, the major difference is that the direction of propagation is perpendicular to the direction of displacement. Thus, if $\mathbf{n}_q$ is taken as the direction of propagation, $\mathbf{n}_{qp}$ is a perpendicular direction of shear displacement and velocity. Therefore, $\mathbf{n}_q \cdot \mathbf{n}_{qp} = 0$.

To account for the perpendicular relation in the case of shear wave, we add 90° or $\pi/2$ to the angle formed by q and x (the detected direction). Thus, equation (12) becomes
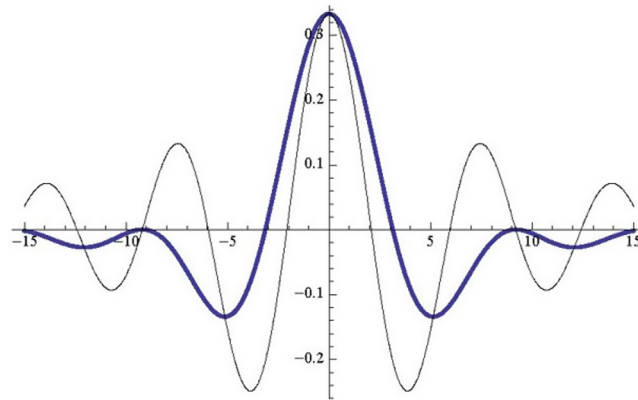
Figure 2. The autocorrelation $B_{vv}(t = 0, \Delta\varepsilon)$ depends on the relative direction of $\Delta\varepsilon$ with respect to the detected component of the velocity vector. In these derivations, the detected direction of motion is taken as the x-axis. The thick line gives the autocorrelation with respect to x, the thin line shows the autocorrelation when $\Delta\varepsilon$ is taken in the perpendicular z-direction. The wavenumber k is set to unity for these curves.

$$(\mathbf{n}_{xqp})^2 = (\mathbf{n}_{qp} \cdot \hat{\mathbf{e}}_x)^2 = \left(\sin\left(\theta + \frac{\pi}{2}\right)\cos\phi \right)^2 = (\cos\theta)^2(\cos\phi)^2, \tag{16}$$

and, following the same logical progression as before, equation (14) becomes

$$Bv_x v_x(\Delta t, \Delta\varepsilon_z) = \frac{(V^2)_{\text{avg}}}{2\pi} \int_{\phi=0}^{2\pi} \int_{\theta=0}^{\pi} (\cos\theta)^2(\cos\phi)^2 \times \cos(\omega_0 \Delta t - k\Delta\varepsilon_z \cos\theta) \sin\theta \mathrm{d}\theta \mathrm{d}\phi$$

$$= (V^2)_{\text{avg}} \left(\cos(\omega_0 \Delta t) \left[\frac{\sin(k\Delta\varepsilon_z)}{k\Delta\varepsilon_z} - \frac{2j_1(k\Delta\varepsilon_z)}{k\Delta\varepsilon_z} \right] \right). \tag{17}$$

In the case where $\Delta\varepsilon$ is taken along the x-axis (the direction of the detected velocity), then $\mathbf{n}_q \cdot \hat{\mathbf{e}}_x \Delta\varepsilon_x = \Delta\varepsilon_x \sin\theta\cos\phi$, the argument in equation (17) becomes $\cos(\omega_0 \Delta t - k\Delta\varepsilon_x \sin\theta\cos\phi)$, and the integration results in

$$Bv_x v_x(\Delta t, \Delta\varepsilon_x) = 2(V^2)_{\text{avg}} \cos(\omega_0 \Delta t) \left[\frac{j_1(k\Delta\varepsilon_x)}{k\Delta\varepsilon_x} + \frac{\sin(k\Delta\varepsilon_x)}{k^3 \Delta\varepsilon_x^3} - \frac{1}{k^2 \Delta\varepsilon_x^2} \right]. \tag{18}$$

The two functions from equations (17) and (18) are shown in figure 2.

The simplicity of equations (17) and (18), basically 'sinc' and 'jinc' spatial functions, leads to a useful practical implementation. An ultrasound or magnetic resonance imaging (MRI) scanner is used to track tissue motion within a region of interest (ROI). This generates a function $v(x)$ along some ROI. The tissue is subjected to multiple shear wave sources that are operating at a frequency typically in the range of 30–1000 Hz. The correlation function B_{vv} is calculated and fit to equation (17) or (18) to estimate the unknown parameter k. Local estimates of k are used to create a map, typically displayed in color, representing the SWS, a measure of the stiffness of the tissue, at different locations.

An efficient estimator for the unknown k in equation (17) is realized by examining the Fourier transform of the autocorrelation function:

$$\mathfrak{I}_x\left\{\frac{\sin(kx)}{kx} - \frac{2j_i(kx)}{kx}\right\} = \sqrt{\frac{\pi}{2}}\left(\frac{s^2}{k^3}\right) \quad \text{for} \quad s \leqslant k, \tag{19}$$

and s is the spatial transform variable. This is a strictly bandlimited function with upper limit of spatial frequency set by k, the unknown wavenumber. The second moment m^2 of the transform is therefore similarly determined by k. From Bracewell, chapter 8, page 143 (1965):

$$\begin{aligned} m_s^2 &= \int_{-k}^{+k}(s^2)\sqrt{\frac{\pi}{2}}\left(\frac{s^2}{2k^3}\right)\mathrm{d}s \\ &= \frac{\sqrt{2\pi}}{5}k^2. \end{aligned} \tag{20}$$

Similarly, the Fourier transform of equation (18)'s spatial term is:

$$\mathfrak{I}_x\{\cdot\} = \frac{s(s-k)}{2k^3} \quad \text{for} \quad 0 < s < k, \tag{21}$$

and the function is a real and even function of s. The second moment for this case is:

$$m_s^2 = \frac{k^2}{5}, \tag{22}$$

Furthermore, it is well known that the second moment of a transform is precisely related to the second derivative of the function at the origin (Bracewell 1965). This can be approximated by a finite difference. Thus:

$$\left|\widehat{k}\right|^2 \cong C\left[\mathrm{Re}\{B\upsilon\upsilon(0)\} - \mathrm{Re}\{B\upsilon\upsilon(\Delta x)\}\right], \tag{23}$$

where $\widehat{k}$ is the estimate, C is a constant equal to $10/(\Delta x^2 \cdot B\upsilon\upsilon(0))$, and the Δx lag and zero lag values of the real part of the autocorrelation at $\Delta t = 0$ from some segment of data are used. A similar expression applies to the estimate using Δz. Since the autocorrelation varies as $\cos(\omega_0\Delta t)$, if desired for noise reduction the data can be taken at integer multiples of $\Delta t = N\pi/\omega_0$ and results can be averaged.

3. Methods

3.1. Numerical simulations

Numerical simulations using finite element analysis were conducted using Abaqus/CAE version 6.14-1 (Dassault Systems, Vélizy-Villacoublay, France) in order to corroborate the gelatin phantom experiments (shell-element analysis), and the breast phantom (3D solid finite element analysis) described in later sections.

3.1.1. Shell-element analysis. The profile of a 3D mesh model of a breast (figure 3(a)) is used to create a 2D geometrical solid model of a homogeneous breast with a hard inclusion simulating a tumor. In order to ensure a full complement of shear waves across different orientations, the boundary conditions were set to have 16 surface traction loads of 10^{-8} Newtons and random initial phase located in approximately equidistant segments of the breast model (figure 3(b)). The model was meshed using approximately 1 500 000 hybrid and quadratic shell elements (figure 3(c)). Power law frequency dependent viscoelastic material properties were chosen to represent tissue. The elastic modulus, density, and viscoelastic parameters assigned
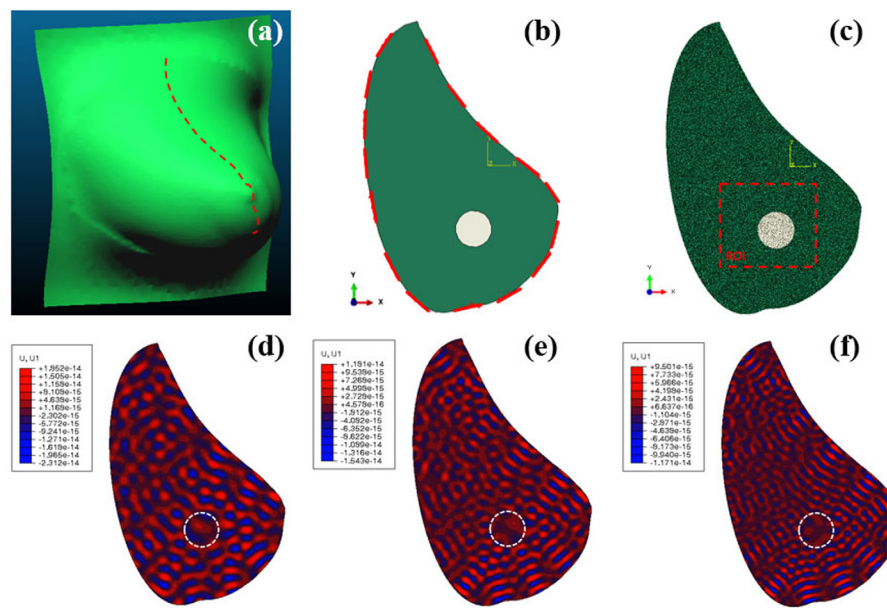
Figure 3. (a) 3D mesh of a breast model. (b) Geometrical model of the breast shaped as a 2D profile of the mesh model in (a) with boundary conditions and loads indicated in Abaqus/CAE. (c) Finite shell-element mesh of (b) with material properties definition in the background and inclusion (diameter = 17 mm), and delimitation of the region on interest. (d)–(f) Displacement field in the *x*-axis for the frequencies of operation: 400 Hz, 500 Hz, and 600 Hz, respectively.

Table 1. Viscoelastic material parameters of the background and inclusion in the 2D finite element model. The power law frequency-dependent model is $g * (\omega) = g_1^* f^{-a}$, where $g * (\omega)$ is the Fourier transform of the non-dimensional shear relaxation function, g_1^* is a complex constant, a is a real constant, and $f = \omega/2\pi$.

|	Density, ρ (kg m^{-3})	Poisson's ratio, v	Young's modulus, E (Pa)	Power law frequency-dependent parameters		
				Real $\{g_1^*\}$	Imag $\{g_1^*\}$	a
Background	998	0.499	5227.2	0.01730	−0.1715	0.936
Inclusion	998	0.499	18 154.8			

to the background and the inclusion are described in table 1. These parameters are in the range of gelatin phantom values extracted using the mechanical testing described in section 3.2. The type of simulation was selected to be steady-state dynamic direct solution for a range of frequencies between 100 Hz and 1000 Hz. This type of analysis calculates the 3D complex sinusoidal steady state solution of displacement and particle velocity of the breast when the defined loads introduce vibrations in the model.

After the simulation was conducted, the complex values of particle velocity were stored for a posterior post-processing step. Figures 3(d)–(f) shows reverberant vector fields within the background and inclusion for different frequencies.

Table 2. Viscoelastic material parameters of the background and inclusion in the 3D finite element model. The power law frequency-dependent model is $g * (\omega) = g_1^* f^{-a}$, where $g * (\omega)$ is the Fourier transform of the non-dimensional shear relaxation function, g_1^* is a complex constant, a is a real constant, and $f = \omega/2\pi$.

| | Density, ρ (kg m^{-3}) | Poisson's ratio, v | Young's modulus, E (Pa) | Power law frequency-dependent parameters | | |
				Real $\{g_1^*\}$	Imag $\{g_1^*\}$	a
Background	998	0.499	20 000	0.004 521	−0.044 82	0.936
Inclusion	998	0.499	40 000			
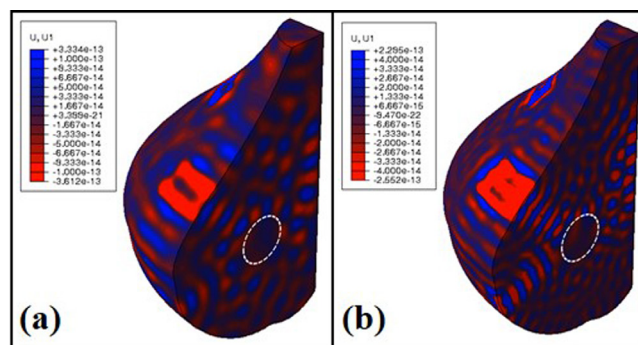
Figure 4. 3D finite element solid model in Abaqus/CAE of the breast with magnitude displacement field of the complex sinusoidal steady-state solution within an interior plane. (a) and (b) Displacement field in the *z*-axis for the frequencies of operation of 450 Hz and 500 Hz, respectively, in the background and inclusion (diameter = 13 mm) regions.

3.1.2. 3D solid finite element analysis. A 3D geometrical solid model of a homogeneous breast with a hard inclusion was created and meshed using approximately 400 000 hybrid and quadratic tetrahedral elements using the shape of the mesh model in figure 3(a). The material properties were chosen according to the specifications of the zerdine breast phantom (model 509, CIRS Inc., Norfolk, Virginia) assigned to the background and inclusion part as described in table 2.

The type of simulation selected was a steady-state dynamic direct solution for two frequencies of operation 450 Hz and 500 Hz. The boundary conditions were set to be zero displacement in the sector that represents the chest wall. In addition, eight surface traction loads were located in approximately equidistant locations across of the breast model in order to produce shear displacement at the frequency of operation. The complex values of particle velocity were stored for post-processing. A profile cut of the model shows reverberant vector fields within the background and inclusion for the frequencies of operation of 450 Hz and 500 Hz (figures 4(a) and (b)).

3.2. Ultrasound experiments

A power amplifier (model 2718, Bruel and Kjaer, Naerum, Denmark), and a digital power amplifier (model LP-2020 A+, Lepai, Bukang, China) driven by a dual channel function generator (model AFG3022B, Tektronix, Beaverton, OR, USA) provided input signals to two mechanical vibration sources (model 4810, Bruel and Kjaer, Naerum, Denmark), and two miniature vibration sources (model NCM02-05-005-4 JB, H2W, Linear Actuator, Santa Clara,

Figure 5. Schematic setup using four external vibration sources to generate a reverberation field inside the breast tissue mimicking phantom.

CA, USA) vibrating at frequencies between 400 and 500 Hz in contact with a gelatin-based and a zerdine breast phantom (model 509, CIRS Inc., Norfolk, Virginia). Inside the gelatin-based phantom, a stiffer cylindrical inclusion 12.6 mm in diameter, embedded in an otherwise homogeneous background, was constructed following the procedure used by Hah *et al* (2012). The phantom with gelatin (300 Bloom Pork Gelatin, Gelatin Innovations Inc., Schiller Park, IL, USA) concentrations of 4% for the background and 7% for the inclusion, was created by heating a mixture of gelatin, 0.7 l of degassed water, 6.3 g of Na-Cl and 1.05 g of agar to 50 °C. The mixture was then cooled to approximately 30 °C and poured into a cubic mold $(14 \times 10 \times 10 \, \text{cm}^3)$ and was then allowed to rest at 4 °C overnight. Before the experiment, this phantom was taken out of its molds and left at room temperature for 3 h. The size and shape of the zerdine phantom simulates a patient in the supine position, and it contains several solid masses that are at least two times stiffer than the background. Lesions range in size from 3 to 10 mm in diameter and are randomly positioned throughout the background. Figure 5 shows the schematic setup using the zerdine breast phantom. Additionally, a Verasonics ultrasound system (V-1, Verasonics Inc., Kirkland, WA, USA), which enables high frame rate acquisition and a coherent plane wave compounding acquisition scheme, and a linear array ultrasound transducer (Model L7-4, Verasonics Inc., Redmond, WA, USA) were used to track the induced displacements using Loupas' estimator (Loupas *et al* 1995). A 3D matrix of IQ data was stored for post-processing. The axial displacements are computed from frame-to-frame analysis of the acquired 3D IQ data. A movie is made and the amplitude and phase of displacement at each pixel are estimated. In all the experiments the center frequency was 5 MHz and the tracking pulse repetition frequency (PRF) is set to acquire at least 20 samples per cycle, i.e. PRF = 20 times the vibration frequency.

3.3. Mechanical measurements

For the gelatin-based phantom materials, compression tests (Zhang *et al* 2007) were performed on three cylindrical samples (approximately 38 mm in diameter and 33 mm in length) made with the same mixtures used to construct the gelatin-based media. A QT/5 mechanical device (MTS Systems Co., Eden Prairie, MN, USA) with a 5 N load cell was used to measure the stress–strain response. The compression rate was adjusted to 0.5 mm s^{-1}. These conventional mechanical measurements were considered the reference when assessing the elasticity properties of the cylindrical phantom.

4. Results

4.1. Numerical simulations

4.1.1. Shell-element analysis. Complex-value displacement frames of the reverberation pattern within an anterior ROI containing the lesion were stored for analysis. Figure 6(a) shows the real part of the displacement pattern for an excitation frequency of 400 Hz in which the background and inclusion can be identified by the global separation size of the peaks and valleys of the interference. Figure 6(b) shows a 2D SWS map obtained by applying our approach to an autocorrelation window ($1.3 \times 1.3\,\mathrm{cm}^2$, equivalent to 150×150 sample points) which is moved to cover the entire ROI. Profiles in the *x* and *y* direction are taken from the 2D correlation, which are in good agreement with theory when compared to the equations (17) and (18) in figures 6(c) and (d), respectively. Subsequently, the second moment approach described in equation (23) is applied to the correlation profiles taking into account the scale factor *C* obtained previously from simulations. The estimation of $\widehat{k}$ in both axes is averaged and used in the calculation of the SWS by $c_s = \omega/\widehat{k}_\mathrm{ave}$.

Results obtained at different frequencies are used to generate average values of SWS in the background and inclusion with respect to the percentage ratio between the wave number λ and the diameter of the inclusion *d*. Then, as shown by figure 7(a), estimations of shear speed tend to approximate ground truth values for smaller λ/d rates. This behavior is expected since the estimation improves as more displacement cycles are used in the cross correlation calculation. In figure 7(b), SWS profiles depicting the background and inclusion values are shown for different values of λ/d rate.

4.1.2. 3D solid finite element analysis. Complex-value displacement frames of the reverberation at 450 Hz and 500 Hz were obtained during simulations. Figure 8(a) shows a profile of the real part of the displacement pattern for 450 Hz excitation frequency. The effects of the viscosity (attenuation) and the boundary conditions influence the quality of the reverberation pattern. The same approach for the calculation of SWS on the shell-element simulation data is applied for the 3D finite element case as shown in figures 8(b) and (c). Average values of SWS reports $c_s = 2.45 \pm 0.1$ m s^{-1} in the background (ground truth $c_s = 2.58$ m s^{-1}) and $c_s = 3.49 \pm 0.26$ m s^{-1} in the inclusion (ground truth $c_s = 3.65$ m s^{-1}).

Some artifacts are seen near the outer boundaries where the assumptions of the isotropic reverberant fields may not hold.

4.2. Ultrasound experiments

4.2.1. Gelatin-based phantom. Figure 9(a) shows the reverberation displacements from the gelatin-based phantom at 400 Hz. Figure 9(b) presents the phase map obtained by the Fourier transform of the displacement pattern through time at each (axial-lateral) location. The B-mode and the SWS images (obtained by applying our approach to a correlation window $1.3 \times 1.3\,\mathrm{cm}^2$ in size, equivalent to 85×85 sample points) are shown in figures 9(c) and (d), respectively. A ROI ($7 \times 7\,\mathrm{mm}^2$) was taken from the background and the inclusion in order to obtain a mean value of each region: 1.22 ± 0.01 m s^{-1}, 2.15 ± 0.13 m s^{-1}, respectively. The SWS result for both regions are in agreement with the elasticity properties obtained with mechanical measurements: 1.32 ± 0.16 m s^{-1}, 2.46 ± 0.21 m s^{-1}, respectively. Finally, figure 9(e) shows the SWS profile for a fixed depth corresponding to figure 9(d).
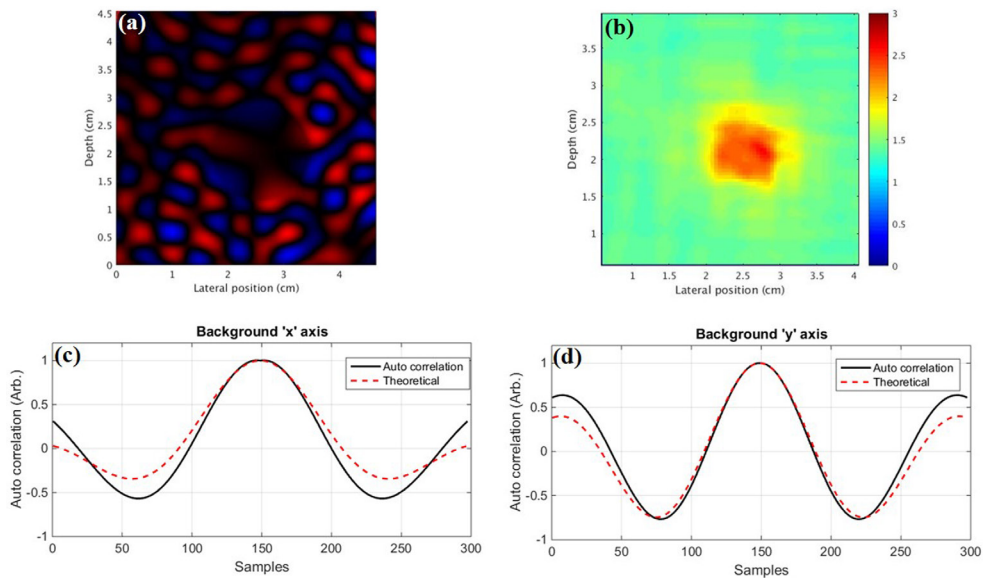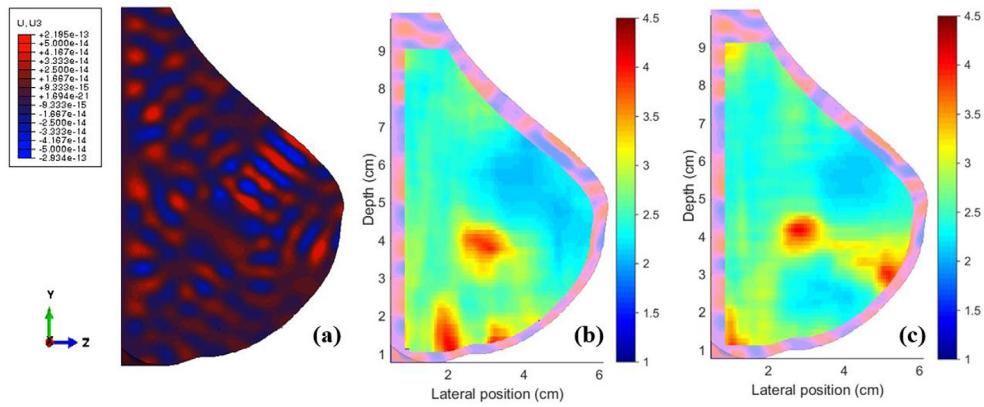
Figure 6. (a) Displacement pattern at 400 Hz obtained using shell-element simulation model in Abaqus/CAE. (b) SWS map calculated from (a) using the second moment algorithm. (c) and (d) Auto correlation pattern extracted from (b) in the *x*- and *y*-axis, respectively.
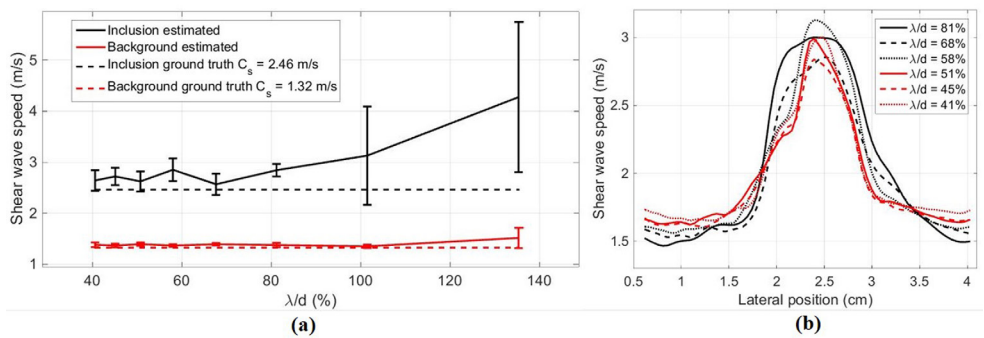

Figure 7. (a) Comparison of SWS estimation using the second moment algorithm in the background and inclusion for various values of λ/d, where $\lambda(m)$ is the wavelength of the excitation, and $d(m)$ is the diameter of the inclusion. (b) SWS profiles showing the background and inclusion for various λ/d.

4.2.2. Zerdine breast phantom. Figure 10 shows the reverberation results from the CIRS breast phantom. The displacement patterns using a vibration frequency of 450 Hz is shown in figure 10(a). Figure 10(b) presents the phase map of the reverberation pattern at 450 Hz; it can be noticed that there are two different wavelengths between 2 and 3 cm depth, which is the region where the inclusion is located (see B-mode image (figure 10(c)). The SWS maps, (obtained by applying our approach to a correlation window $1.3 \times 1.3\,cm^2$ in size) overlaying the B-mode image, are shown in figure 10(d). A ROI ($7 \times 7\,mm^2$) was taken from the background and the inclusion in order to obtain a mean value for each region: $2.28 \pm 0.14\,m\,s^{-1}$,

Figure 8. (a) 2D profile of the 3D displacement pattern of the breast interior at 450 Hz, obtained using Abaqus/CAE. (b) and (c) SWS map obtained from (a) using the second moment algorithm for frequencies of 450 Hz and 500 Hz, respectively.
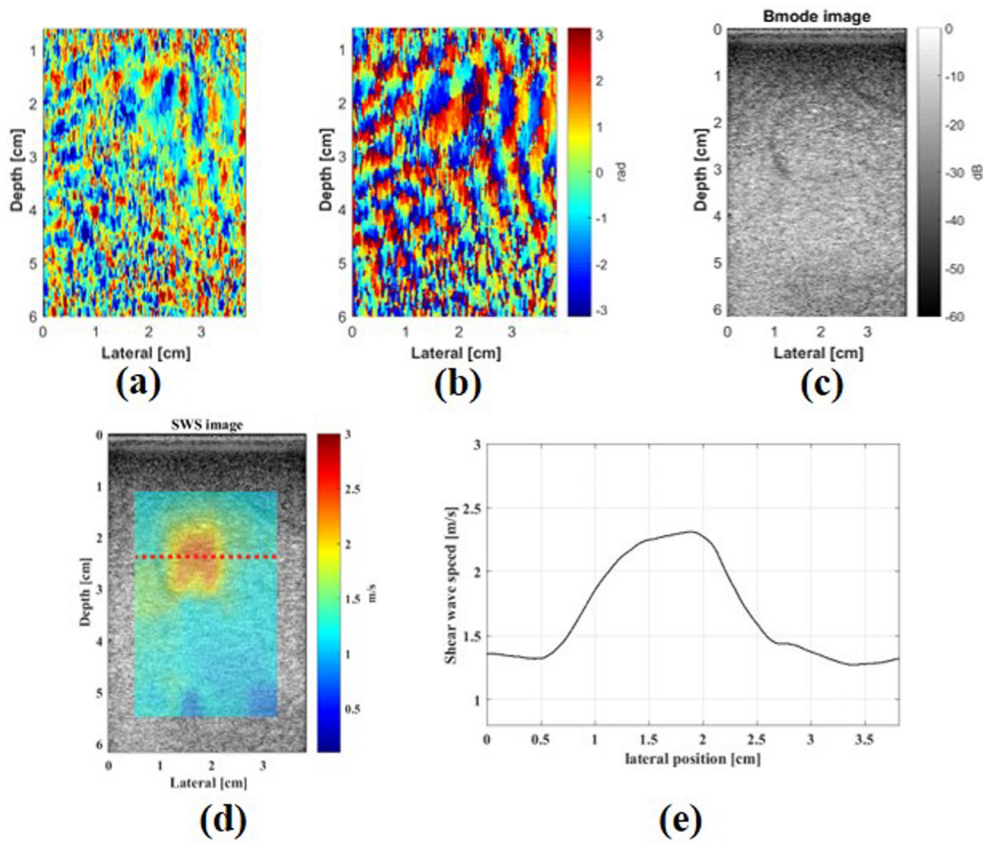

Figure 9. (a) Displacement pattern at 400 Hz obtained from the gelatin phantom. (b) Phase map of (a). (c) B-mode image. (d) SWS map calculated from (a) using the second moment algorithm; the red dotted line illustrates the depth of the SWS profile. (e) SWS profile across the lesion.
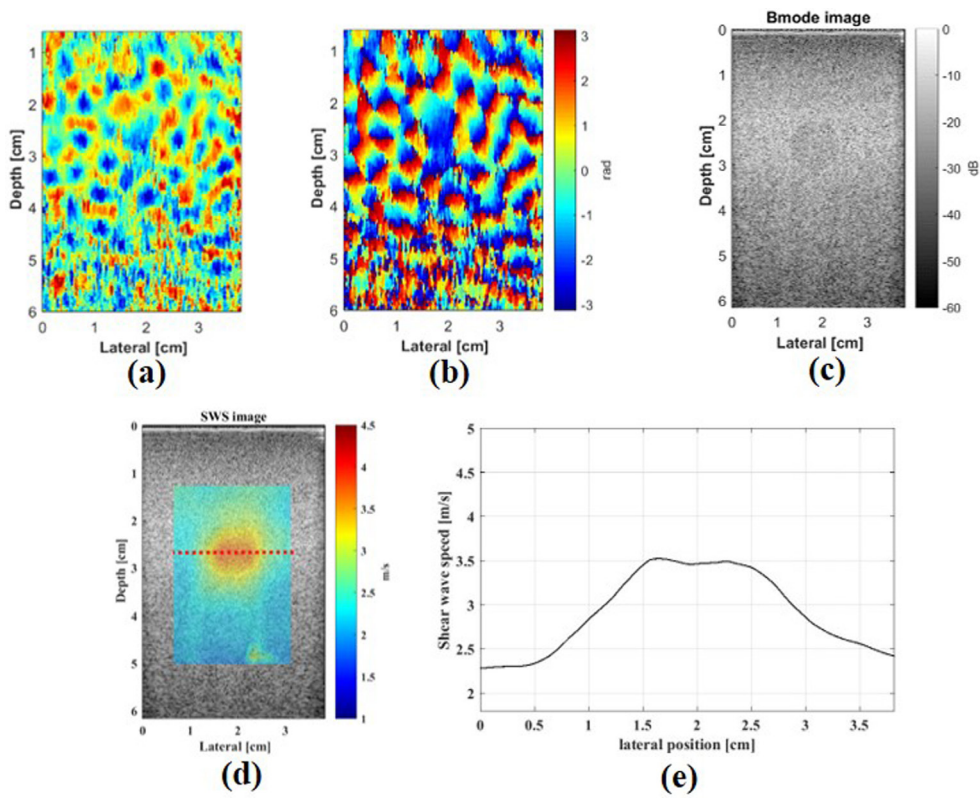
Figure 10. (a) Displacement pattern at 450 Hz, obtained from the zerdine breast phantom. (b) Phase map of (a). (c) B-mode image. (d) SWS map calculated from (a) using the second moment algorithm at 450 Hz; the red dotted line illustrates the location of the SWS profile. (e) SWS profile at a fixed depth through the lesion across the lateral direction from (d).
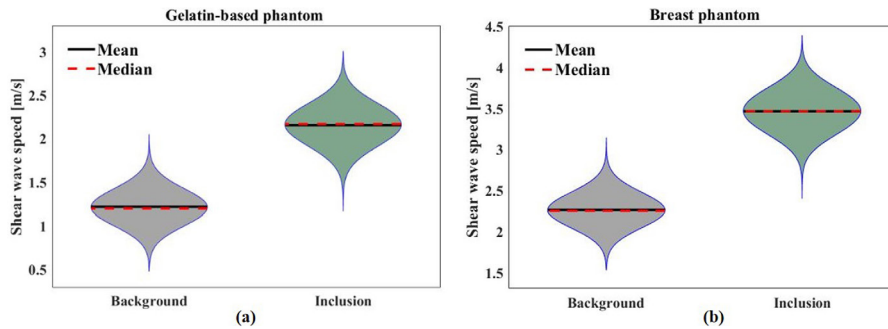
Figure 11. Violin plots showing the SWS estimate summary for the background and inclusion ROI. (a) and (b) SWS summary for the gelatin-based phantom at 400 Hz and the zerdine breast phantom at 450 Hz, respectively.

3.43 $\pm$ 0.18 m s^{-1} for 450 Hz, respectively. The SWS result for the background is in agreement with the elasticity properties specified by the CIRS manufacturer: 2.58 $\pm$ 0.32 m s^{-1}. For the SWS result at the inclusion, the phantom manufacturer only reported that the inclusion stiffness is, at least, two times higher than the background. Thus, the SWS result for the inclusion is in agreement with that information as well. Finally, figure 10(e) shows the SWS profile for a fixed depth corresponding to figure 10(d).

Figure 11 shows a SWS estimate summary, background and inclusion ROI for the gelatin-based and breast phantoms. The width of the violin plots shows the probability density of the data at different values. The black and red dashed lines represent the mean and median of the data.

5. Discussion

There are a number of advantages to utilizing the framework of reverberant fields. First, the presence of reflections from boundaries and internal inhomogeneities is unavoidable in some common elastographic approaches, and these reflections plus the application of multiple sources and mode conversions can all contribute to the creation of the reverberant shear wave field. Once established, the characteristics can be exploited to estimate the underlying shear wave phase velocity. Secondly, the expected value of the autocorrelation function has been derived assuming only one vector component of detected velocity. This represents the simplest and most rapid data acquisition for both ultrasound and MRI, as additional transmit directions (in ultrasound) or additional phase encoding (in MRI) are required to determine additional vector components of shear wave velocity, and these are unnecessary in the framework developed herein. Thirdly, the need to verify a principle direction of wave propagation is eliminated in the reverberant framework as the underlying mathematics account for a superposition of waves. Fourthly, the need for explicit knowledge of boundary conditions or second derivatives that are essential in some inverse approaches (Doyley 2012) are avoided in the reverberant approach.

A practical issue for clinicians concerns the time required for data acquisition and processing of the estimator images, particularly for ultrasound systems that are intended for real time operation. High frame rate ultrasound scanning and high complexity shear wave algorithms are already implemented on a number of ultrasound systems, so the limiting factor may be the time required to acquire a satisfactory estimate of the reverberant autocorrelation function. For 100 Hz shear waves, capturing one cycle of displacements takes 1/100 s, of course more or less could be necessary depending on noise and unwanted tissue motion, however this illustration points to the possibility of reverberant elastography frame rates that are perceived as real time.

Since the reverberant shear wave framework is at an early stage and the results are preliminary, a number of issues are left for further research. One practical issue concerns the behavior of estimates in situations where the field fails to approach the diffuse or reverberant ideal. An extreme deviation would be where waves exist along only one axis, for example with a pair of interfering plane waves aligned with the *z*-axis of figure 1. In this extreme case the autocorrelation function would be a $\cos(k\Delta z)$ function, the Fourier transform a delta function pair at $\pm k$, and the second moment equal to k^2 instead of $k^2\left(\sqrt{2\pi}/5\right)$ as in equation (20). In this case the estimate of k would be overestimated by a factor of 2, and correspondingly c would be underestimated.

However, the exact amount of error depends on the precise orientation of the standing wave in this simple example. A more comprehensive determination of the degradation or deviation from the model as a function of organ size, attenuation, frequency, and shear wave sources, remains to be quantified. In addition, the performance of estimators of SWS as a function of the same parameters requires detailed assessment. Furthermore, the ideal reverberant field as expressed in equations (4)–(18) does not consider a number of wave phenomena which could exist in practice, including longitudinal shear waves. These can be created along the axis of symmetry near a translating source (Carstensen *et al* 2008, Catheline and Benech 2015) and would add a localized vector component to the displacement. The presence of an absorbing surface also degrades the isotropic diffuse field assumption near that surface (Pierce 1981). Finally, multi-frequency versions of the approach can be implemented to assess the frequency dependence of SWS and hence the dispersion and viscoelastic properties. These practical issues can be assessed within the framework of the reverberant shear wave field and are left for future research.

Acknowledgments

References

Abramowitz M and Stegun I A 1964 *Handbook of Mathematical Functions with Formulas, Graphs, and Mathematical Tables* (Washington, DC: US Government Printing Office)
Baddour N 2011 Multidimensional wave field signal theory: mathematical foundations *AIP Adv.* **1** 0221201
Bracewell R N 1965 *The Fourier Transform and its Applications* (New York: McGraw-Hill)
Brum J, Catheline S, Benech N and Negreira C 2015 Quantitative shear elasticity imaging from a complex elastic wavefield in soft solids with application to passive elastography *IEEE Trans. Ultrason. Ferroelectr. Freq. Control* **62** 673–85
Carstensen E L, Parker K J and Lerner R M 2008 Elastography in the management of liver disease *Ultrasound Med. Biol.* **34** 1535–46
Castaneda B, An L, Wu S, Baxter L L, Yao J L, Joseph J V, Hoyt K, Strang J, Rubens D J and Parker K J 2009 *Prostate Cancer Detection Using Crawling Wave Sonoelastography* ed S A McAleavey and J D'Hooge (Lake Buena Vista, FL: SPIE) p 726513
Catheline S and Benech N 2015 Longitudinal shear wave and transverse dilatational wave in solids *J. Acoust. Soc. Am.* **137** EL200–5
Catheline S, Benech N, Brum J and Negreira C 2008 Time reversal of elastic waves in soft solids *Phys. Rev. Lett.* **100** 064301
Cook R K, Waterhouse R V, Berendt R D, Edelman S and Thompson M C 1955 Measurement of correlation coefficients in reverberant sound fields *J. Acoust. Soc. Am.* **27** 1072–7
Deffieux T, Gennisson J L, Bercoff J and Tanter M 2011 On the effects of reflected waves in transient shear wave elastography *IEEE Trans. Ultrason. Ferroelectr. Freq. Control* **58** 2032–5
Doyley M M 2012 Model-based elastography: a survey of approaches to the inverse elasticity problem *Phys. Med. Biol.* **57** R35–73
Engel A J and Bashford G R 2015 A new method for shear wave speed estimation in shear wave elastography *IEEE Trans. Ultrason. Ferroelectr. Freq. Control* **62** 2106–14
Fai Y, Levinson S F, Dongshan F and Parker K J 1998 Feature-adaptive motion tracking of ultrasound image sequences using a deformable mesh *IEEE Trans. Med. Imaging* **17** 945–56

Fu D, Levinson S F, Graceswki S M and Parker K J 1999 Solution of the inverse problem in sonoelastography using an iterative forward approach *Ultrasonic Imaging and Tissue Characterization Symp.* pp 61–2

Gallot T, Catheline S, Roux P, Brum J, Benech N and Negreira C 2011 Passive elastography: shear-wave tomography from physiological-noise correlation in soft tissues *IEEE Trans. Ultrason. Ferroelectr. Freq. Control* **58** 1122–6

Hah Z, Hazard C, Mills B, Barry C, Rubens D and Parker K 2012 Integration of crawling waves in an ultrasound imaging system. Part 2: signal processing and applications *Ultrasound Med. Biol.* **38** 312–23

Loupas T, Peterson R B and Gill R W 1995 Experimental evaluation of velocity and power estimation for ultrasound blood flow imaging, by means of a two-dimensional autocorrelation approach *IEEE Trans. Ultrason. Ferroelectr. Freq. Control* **42** 689–99

Manduca A, Lake D S, Kruse S A and Ehman R L 2003 Spatio-temporal directional filtering for improved inversion of MR elastography images *Med. Image Anal.* **7** 465–73

McLaughlin J and Renzi D 2006 Shear wave speed recovery in transient elastography and supersonic imaging using propagating fronts *Inverse Problems* **22** 681–706

Oliphant T E, Manduca A, Ehman R L and Greenleaf J F 2001 Complex-valued stiffness reconstruction for magnetic resonance elastography by algebraic inversion of the differential equation *Magn. Reson. Med.* **45** 299–310

Parker K J 2013 *Imaging in Medical Diagnosis and Therapy* (Boca Raton, FL: CRC Press) p xvii, 331 p

Parker K J, Doyley M M and Rubens D J 2011 Imaging the elastic properties of tissue: the 20 year perspective *Phys. Med. Biol.* **56** R1–29

Parker K J and Lerner R M 1992 Sonoelasticity of organs: shear waves ring a bell *J. Ultrasound Med.* **11** 387–92

Parker K J and Maye B A 1984 Partially coherent radiation from reverberant chambers *J. Acoust. Soc. Am.* **76** 309–13

Parker K J, Taylor L S, Gracewski S and Rubens D J 2005 A unified view of imaging the elastic properties of tissue *J. Acoust. Soc. Am.* **117** 2705–12

Pengfei S, Heng Z, Manduca A, Urban M W, Greenleaf J F and Shigao C 2012 Comb-push ultrasound shear elastography (CUSE): a novel method for two-dimensional shear elasticity imaging of soft tissues *IEEE Trans. Med. Imaging* **31** 1821–32

Pierce A D 1981 *McGraw-Hill Series in Mechanical Engineering* (New York: McGraw-Hill)

Ringleb S I, Chen Q, Lake D S, Manduca A, Ehman R L and An K N 2005 Quantitative shear wave magnetic resonance elastography: comparison to a dynamic shear material test *Magn. Reson. Med.* **53** 1197–201

Romano A J, Bucaro J A, Ehnan R L and Shirron J J 2000 Evaluation of a material parameter extraction algorithm using MRI-based displacement measurements *IEEE Trans. Ultrason. Ferroelectr. Freq. Control* **47** 1575–81

Roux P, Sabra K G, Kuperman W A and Roux A 2005 Ambient noise cross correlation in free space: theoretical approach *J. Acoust. Soc. Am.* **117** 79–84

Sinkus R, Lorenzen J, Schrader D, Lorenzen M, Dargatz M and Holz D 2000 High-resolution tensor MR elastography for breast tumour detection *Phys. Med. Biol.* **45** 1649–64

Taylor L S, Porter B C, Rubens D J and Parker K J 2000 Three-dimensional sonoelastography: principles and practices *Phys. Med. Biol.* **45** 1477–94

Tzschatzsch H, Guo J, Dittmann F, Hirsch S, Barnhill E, Johrens K, Braun J and Sack I 2016 Tomoelastography by multifrequency wave number recovery from time-harmonic propagating shear waves *Med. Image Anal.* **30** 1–10

Tzschatzsch H, Ipek-Ugay S, Guo J, Streitberger K J, Gentz E, Fischer T, Klaua R, Schultz M, Braun J and Sack I 2014 *In vivo* time-harmonic multifrequency elastography of the human liver *Phys. Med. Biol.* **59** 1641–54

Tzschatzsch H, Ipek-Ugay S, Trong M N, Guo J, Eggers J, Gentz E, Fischer T, Schultz M, Braun J and Sack I 2015 Multifrequency time-harmonic elastography for the measurement of liver viscoelasticity in large tissue windows *Ultrasound Med. Biol.* **41** 724–33

Van Houten E E, Miga M I, Weaver J B, Kennedy F E and Paulsen K D 2001 Three-dimensional subzone-based reconstruction algorithm for MR elastography *Magn. Reson. Med.* **45** 827–37

Zhang M, Castaneda B, Wu Z, Nigwekar P, Joseph J V, Rubens D J and Parker K J 2007 Congruence of imaging estimators and mechanical measurements of viscoelastic properties of soft tissues *Ultrasound Med. Biol.* **33** 1617–31